A numerical study of heat island flows: Stationary solutions

Thierry Dubois[*,†] and Rachid Touzani

*Laboratoire de Mathématiques, UMR CNRS 6620, Université Blaise Pascal (Clermont-Ferrand 2),
63177 Aubière Cedex, France*

SUMMARY

We present two-dimensional numerical simulations of a natural convection problem in an unbounded domain. The flow circulation is induced by a heat island located on the ground and thermal stratification is applied in the vertical direction. The main effect of this stably stratified environment is to induce the propagation of thermal perturbations in the horizontal direction far from the local thermal source. Numerical stationary solutions at $Ra \leqslant 10^5$ are computed in large elongated computational domains: convergence with respect to the domain sizes is investigated at different resolutions. On fine grids, with mesh size $h = \frac{1}{128}$, a thermal sponge layer is added at the vertical boundaries: this *local damping* technique improves the convergence with respect to the domain length. Boussinesq equations are discretized with a second-order finite volume scheme on a staggered grid combined with a second-order projection method for the time integration. Copyright © 2008 John Wiley & Sons, Ltd.

1. INTRODUCTION

In this paper we present numerical simulations of a particular type of thermal fluid flows, namely, we are concerned with the so-called *heat island* flows [1], i.e. fluid flows where natural convection is generated by a local variation of temperature, thus inducing buoyancy effect. This phenomenon appears in the presence of heat stratification that stabilizes the fluid flow. The present model is generally used to study environment problems such as urban heat island [2, 3]. Heat island fluid flows occur in open configurations, which require, from the mathematical viewpoint, their study in unbounded domains. In practice, numerical simulations are carried out in *large* but bounded computational domains for which the appropriate design of boundary conditions must be investigated.

---

*Correspondence to: Thierry Dubois, Laboratoire de Mathématiques, Université Blaise Pascal, 63177 Aubière Cedex, France.
†E-mail: Thierry.Dubois@math.univ-bpclermont.fr

For this problem, the heat island perturbation generates an ascending flow circulation that develops mainly in an area surrounding the heated element. The vertical stratification limits this effect by restricting the vertical flow circulation that is forced to extend in the horizontal direction. At low Rayleigh numbers the flow is stationary and the thermal circulation consists in a symmetric and centered multi-cell pattern. Above the heat source, a zone of colder air is observed. When the Rayleigh number is sufficiently large, the symmetry is broken: oscillations with respect to the center of the heat island evolve in a time periodic regime. The numerical study of the development of instabilities and the detection of successive transitions from steady-state to time-dependent flows, namely, periodic, quasi-periodic and finally chaotic (turbulent), is our main motivation for this problem. A preliminary study is presented in [4].

In most studies devoted to natural convections in a stratified environment, the flow fills a closed area or is driven by an inflow velocity imposed on one of the vertical boundaries (see [5–7], for instance). In the latter case, outflow boundary conditions of Neumann type are appropriate. Their aim is to model an open situation for which the flow is free to move through the exit plane, outside the computational domain. For the computation of natural convection flows driven by a local heated source in unbounded domains, the far-field behavior of the solution is generally not known (see [8] and the references therein). Owing to the stratified environment of the heat island problem, thermal perturbations are propagated in the horizontal direction far from the heated element. The vertical boundaries can then be either inflow or outflow boundaries, even both. The numerical simulations are carried out in large but bounded computational domains on which artificial boundary conditions are applied. Therefore, the numerical simulations depend not only on the numerical parameters such as the mesh size and the time step but also on the domain size, generally expressed in terms of the distance from the heated element.

When seeking transitions from steady to unsteady solutions with respect to a flow parameter, the reliability of the numerical results strongly depends on the accuracy of the simulations (see [9], for instance). Therefore, for the problem considered in this paper, estimating the effect of the computational domain length and height on the numerical solutions is essential. The elevation of the heat island is reduced by the vertical stratification so that the domain height necessary to obtain accurate numerical solutions is not large. In this context, the numerical simulations are performed in *very elongated* domains. For various Rayleigh numbers and spatial resolutions, we attempt to achieve a thorough investigation of the dependency of the numerical results on the computational domain length and height. For such a study, we chose to focus on the computation of stationary solutions. Indeed, steady-state solutions are more appropriate than time-dependent solutions as they offer a large choice of characteristic values that can be used in order to compare simulations performed with different parameters. Our main objective is to provide reference solutions. These results provide a background for further studies and analysis of heat island flows.

This approach is feasible on coarse to moderately fine grids ($h \leqslant \frac{1}{64}$). However, despite the increase in computational resources, direct numerical simulation on finer grids remains unreachable. In order to overcome this difficulty, we propose to apply a thermal sponge layer in the vicinity of the vertical boundaries: the temperature equation is locally modified so that the convective terms are *smoothly* damped in the vicinity of the vertical boundaries. Boundary conditions with a sponge are classically employed in computational electromagnetics [10, 11] and in simulations of compressible turbulent flows [12, 13]. We show that this technique is well suited for the numerical simulations of heat-island-type flows at Rayleigh numbers $Ra \leqslant 10^5$.

The outline of this paper is as follows. In the following section, we describe the set of equations that govern the fluid flow in a heat island as well as the domain geometry and boundary conditions.

In particular, we express the equations in a nondimensional form that involves two parameters, the Rayleigh number and a thermal stratification coefficient. We show that a specific choice of relevant parameters is to be made here for the heat island flow. Section 3 describes approximations in closed domains. Two approaches are used: the former relies on the use of *very large* computational domains without any particular treatment at the domain exits, whereas the latter introduces thermal sponge layers acting in the vicinity of the vertical boundaries. Section 4 presents the space and time discretization schemes. Preliminary numerical results were obtained by Touzani [14] using a finite element method coupled with a penalty method to impose the incompressibility constraint. Here, we use a second-order finite volume scheme on a staggered grid for space discretization and a second-order projection method for the time integration of the resulting system of differential equations. Section 5 gives numerical results. Numerical simulations in a square differentially heated cavity are first performed to check the code accuracy. Stationary solutions to the heat island problem at $Ra \leqslant 10^5$ are obtained in *very elongated* computational domains and are used as references to validate the sponge technique applied to the heat equation. Accurate stationary solutions are then computed with this approach: characteristic values are listed for reference. Finally, conclusions are drawn and perspectives for future works on this problem are discussed.

2. DESCRIPTION OF THE PROBLEM

2.1. The physical problem

We consider a fluid that fills the half plane $\{\mathbf{x}^\star = (x^\star, y^\star) \in \mathbb{R}^2; y^\star > 0\}$. Here and in the sequel we shall append a superscript $\star$ to all physical dependent and independent variables, the notation without $\star$ being reserved to nondimensional variables. The fluid is initially at rest and is thermally stratified in the vertical direction, namely the velocity field $\mathbf{u}^\star = (u^\star, v^\star)$ and the potential temperature $T^\star$ satisfy, at time $t^\star = 0$,

$$\mathbf{u}^\star = \mathbf{0} \tag{1}$$

$$T^\star = T_0 + \alpha_s y^\star \tag{2}$$

where $T_0 > 0$ is the potential temperature at the ground and $\alpha_s > 0$ is the thermal stratification coefficient.

In order to generate a flow, a local temperature of intensity $T_1 > T_0$ is applied on a source line $Q^\star = (-\delta/2, \delta/2)$, $\delta > 0$, located on the ground (see Figure 1), that is, we impose

$$T^*(\mathbf{x}^*, t^*) = T_0 + \frac{(T_1 - T_0)}{2} \left(\tanh\left(\frac{2x^* + \delta}{2\delta\zeta}\right) - \tanh\left(\frac{2x^* - \delta}{2\delta\zeta}\right) \right) \tag{3}$$

for all $\mathbf{x}^* \in \mathbb{R}^2 \cap \{y^* = 0\}$ and for all time $t^* > 0$. Note that this thermal perturbation is constant in time and is a regularized version of a heat-island-type perturbation (see [3], for instance) for which a constant and uniform temperature would be applied on the heated element $Q^\star$. The parameter $\zeta > 0$ in (3) is used to set the sharpness of the temperature gradient $\partial T^* / \partial x^*$ near the plate boundaries $|x^*| = \delta/2$ at the ground level $y^* = 0$. In this study, the value $\zeta = 2.5 \times 10^{-2}$ is used.

Owing to perturbation (3), a thermal plume develops above the heated plate $Q^\star$. Natural convection induces an ascending flow circulation, whereas the gravity force and the vertical stratification limit the development of flow structures in the vertical direction. As a consequence of these opposite forces, thermal perturbations are propagated in the horizontal direction at long distance,
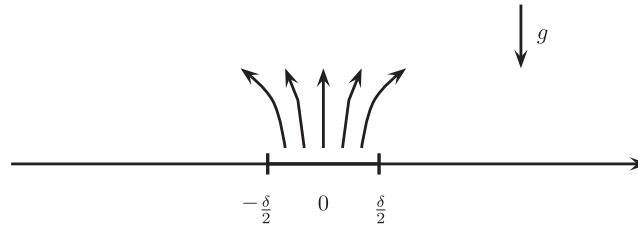
Figure 1. Heat island perturbation.

far from the heated element. We may then expect that the solutions will decay *rapidly* in the vertical direction and *very slowly* in the horizontal one. The main difficulty for this problem, as far as numerical simulations are concerned, resides in a suitable design of boundary conditions in order to properly reproduce the behavior of the far-field solutions. Indeed, errors in the numerical approximation at long distance from the heated plate may reduce the accuracy of simulations in the region surrounding the heated element.

2.2. The governing equations

We consider the set of equations describing a two-dimensional thermal flow assuming Boussinesq approximation. Let us recall that this one stipulates that for small temperature differences, the density variations are more significant in the gravity acceleration term than in others.

Velocity $\mathbf{u}^*$, pressure p^*, density ρ^* and potential temperature T^* satisfy the set of equations

$$\frac{\partial \mathbf{u}^*}{\partial t^*} - v\Delta^* \mathbf{u}^* + \boldsymbol{\nabla}^* \cdot (\mathbf{u}^* \otimes \mathbf{u}^*) + \frac{1}{\rho_0} \boldsymbol{\nabla}^* p^* = -\frac{\rho^*}{\rho_0} g \mathbf{e}_2 \tag{4}$$

$$\boldsymbol{\nabla}^* \cdot \mathbf{u}^* = 0 \tag{5}$$

$$\frac{\partial T^*}{\partial t^*} - \kappa\Delta^* T^* + \boldsymbol{\nabla}^* \cdot (\mathbf{u}^* T^*) = 0 \tag{6}$$

$$\mathbf{u}^*(\mathbf{x}^*, 0) = \mathbf{0}, \quad T^*(\mathbf{x}^*, 0) = T_0 + \alpha_s y^* \tag{7}$$

where the physical constants are the kinematic viscosity v, the thermal diffusivity κ and the modulus of gravity acceleration g. The unit vector in the vertical direction is denoted by $\mathbf{e}_2$, namely $\mathbf{e}_2 = (0, 1)$.

For these type of flows, we have adopted the approximation that compressibility is expressed by a dilatation equation. Therefore, density is related to the temperature variations with respect to the reference state (T_0, ρ_0), by the following equation:

$$\rho^* = \rho_0(1 - \beta(T^* - T_0)) \tag{8}$$

where β is the thermal expansion coefficient. Equations (4)–(8) are to be considered in the infinite domain $\mathbb{R} \times \mathbb{R}^+$ where the line $y^* = 0$ contains the heated plate $Q^* = (-\delta/2, \delta/2)$. Such a problem with appropriate behavior at infinity is well suited for generating a heat island flow in the vicinity of the heated plate if a thermal stratification is given.

The boundary condition (3) has an effect of generating, in the neighborhood of the plate Q^*, a temperature plume with a shape and an intensity depending on the system parameters.

2.3. Nondimensional form of the equations

In order to normalize the problem, we introduce as usual reference values for temperature $T_r = T_1 - T_0$, length $L_r = \delta$ and velocity $U_r = \sqrt{g\beta L_r T_r}$. Reference values for time and pressure can then be deduced by $t_r = L_r/U_r$ and $p_r = \rho_0 U_r^2$, respectively. We define nondimensional space and time variables by $\mathbf{x} = \mathbf{x}^*/L_r$ and $t = t^*/t_r$. In terms of these nondimensional variables, the heated plate reads $Q = (-\frac{1}{2}, \frac{1}{2})$. The nondimensional variables

$$\mathbf{u} = \frac{\mathbf{u}^*}{U_r}, \quad T = \frac{T^* - T_0}{T_r} \quad \text{and} \quad p = \frac{p^* + \rho_0 g y^*}{p_r} \tag{9}$$

satisfy in $\mathbb{R} \times \mathbb{R}^+$ and for $t > 0$ the following system of equations:

$$\frac{\partial \mathbf{u}}{\partial t} - \sqrt{\frac{Pr}{Ra}} \Delta \mathbf{u} + \nabla \cdot (\mathbf{u} \otimes \mathbf{u}) + \nabla p = T \mathbf{e_2} \tag{10}$$

$$\nabla \cdot \mathbf{u} = 0 \tag{11}$$

$$\frac{\partial T}{\partial t} - \frac{1}{\sqrt{Ra\,Pr}} \Delta T + \nabla \cdot (\mathbf{u}T) = 0 \tag{12}$$

$$\mathbf{u}(\mathbf{x}, 0) = \mathbf{0}, \quad T(\mathbf{x}, 0) = \alpha y \tag{13}$$

where $\alpha = \alpha_s L_r / T_r$. The Prandtl and Rayleigh numbers are, respectively, defined by

$$Pr = \frac{\nu}{\kappa} \quad \text{and} \quad Ra = \frac{g\beta L_R^3 T_R}{\nu\kappa}$$

The nondimensional form of the boundary condition (3) reads

$$T(\mathbf{x}, t) = \frac{1}{2}\left(\tanh\left(\frac{2x+1}{2\zeta}\right) - \tanh\left(\frac{2x-1}{2\zeta}\right)\right) \quad \text{for } \mathbf{x} = (x, 0) \tag{14}$$

To simplify, we set the Prandtl number that characterizes the fluid to its value for the air, $Pr = 0.71$. Therefore, the system of Equations (10)–(13) depends on two parameters Ra and α.

For a fixed stratification coefficient α, when the Rayleigh number is increased the solutions of (10)–(13) are expected to evolve from stationary to chaotic (turbulent) ones following a Hopf bifurcation scheme. The critical value of Ra corresponding to the first bifurcation, i.e. transition from a steady state to a time periodic signal, may depend on the value of the stratification coefficient. Preliminary results on coarse grids and with $\alpha = 1$ are presented in [4]: stationary solutions are found at $Ra = 10^5$ and 2.5×10^5, whereas a time periodic solution is obtained at $Ra = 5 \times 10^5$. For natural convection flows driven by a local heated source in unbounded domains, the reliability of numerical simulations depends on the numerical parameters as the mesh size and on the computational domain (see [15]).

In this paper we focus on stationary solutions and study their dependency on the size of the computational domain for a stratification coefficient set to unity. Steady-state solutions are appropriate for such investigations as they offer a large choice of characteristic values useful to estimate the convergence rate with respect to any parameters.

3. APPROXIMATION IN CLOSED DOMAIN

3.1. Large elongated domain

Clearly, problem (10)–(14) is difficult to handle numerically in an unbounded domain. We choose to approximate $\mathbb{R} \times \mathbb{R}^{+}$ by a rectangle $\Omega = (-L/2, L/2) \times (0, H)$ with L large enough (see Figure 2) and we denote by Γ its boundary. A simple and naive approach would consist in imposing conditions on Γ consistent with the initial condition (13) and the boundary condition (14). Therefore, Equations (10)–(13) are supplemented with the boundary conditions

$$\mathbf{u}(\mathbf{x}, t) = 0, \quad \mathbf{x} \in \Gamma \tag{15}$$

$$T(\mathbf{x}, t) = \frac{1}{2} \left(\tanh \left(\frac{2x + 1}{2\zeta} \right) - \tanh \left(\frac{2x - 1}{2\zeta} \right) \right), \quad \mathbf{x} \in \Gamma_0 = \{\mathbf{x} \in \Gamma; y = 0\} \tag{16}$$

$$T(\mathbf{x}, t) = \alpha y, \quad \mathbf{x} \in \Gamma \setminus \Gamma_0 \tag{17}$$

for all time $t > 0$.

Such conditions can be enforced only if the domain lengths L and H are large enough so that their change has a negligible effect on the solution. As it was previously mentioned, the gravity force and the stratified profile (17) tend to push the flow down to the ground, limiting the vertical convection. Therefore, the flow variables have a rapid decay with respect to the elevation y, so that the domain height H does not need to be too large. The heat island perturbation generates an ascending flow circulation that is essentially local. On the other hand, thermal perturbations are convected in the horizontal direction at long distance far from the heated source line. Therefore, very elongated computational domains have to be considered, that is $L \gg H$ and $L \gg 1$, in order to produce accurate solutions.

3.2. A truncated temperature equation

We shall see in the development of this study that the above approach is very consuming in terms of computational resources inducing strong limitations on the allowable grid resolution. Indeed, if the domain length L is not large enough, artificial boundary layers develop at the domain boundaries $|x| = L/2$ inducing an overestimation of the flow variables. These numerical errors deteriorate the accuracy of the solutions in the central area where most of the flow dynamics take place. An appropriate design of the behavior of the solution close to these boundaries is necessary in order to relax the condition $L \gg 1$ on the domain length. To do so, we propose to limit the horizontal propagation of the thermal perturbation by damping the convective terms
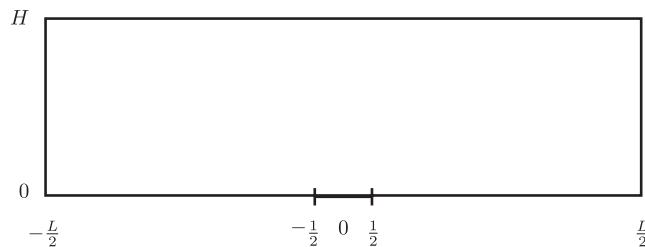

Figure 2. Computational domain $\Omega = (-L/2, L/2) \times (0, H)$.

in the temperature equation in sponge layers close to the domain exits $|x| = L/2$. The nonlinear convection term in (12) is multiplied by a filter function

$$\psi_\gamma(x) = e^{-\gamma(2|x|/\sigma L)^p} \tag{18}$$

where $\sigma \in (0, 1)$ and $p \geqslant 1$. This yields the modified heat equation

$$\frac{\partial T}{\partial t} - \frac{1}{\sqrt{Ra\,Pr}} \Delta T + \psi_\gamma(x) \nabla \cdot (\mathbf{u}T) = 0 \tag{19}$$

For the sake of simplicity, we use the same notation T for the *truncated* and *standard* temperatures, respectively, solution of (19) and (12). The former corresponds to the choice of $\gamma = 1$ and the latter to $\gamma = 0$.

The filter function ψ_γ rapidly decays when $|x| \approx L/2$, whereas $\psi_\gamma \longrightarrow 1$ in the center of the computational domain, thus reducing to a classical convective term. The effect of ψ_γ is to introduce a *sponge layer*, close to the vertical boundaries, where the convection of temperature is smoothly damped through the outflow. As we will see in Section 5, such a treatment allows one to significantly reduce the size of the computational domain Ω required to reach a given accuracy.

This approach, although different in its implementation, is similar to the perfectly matched layer method used in computational electromagnetics and introduced by Berenger [10]. Boundary conditions with a sponge are also commonly used for the numerical simulations of compressible turbulent flows as jet flows, for instance, [13]. For these problems, the solution is driven to a specified outflow state by adding in the sponge layer a *cooling* term to the right-hand side of the equations. We found that our method, for the heat island problem (10)–(14), is less sensitive to the parameters involved in the definition of the sponge functions.

3.3. A model formulated in terms of temperature fluctuations

By noting that a stratified profile of the temperature can be expressed in the momentum equation as a gradient term, we decompose the potential temperature T into $T = \alpha y + \theta$, which introduces the temperature fluctuation θ. By reporting this decomposition into (10), (11), (19) and (13), recalling that $\mathbf{u} = (u, v)$ and, introducing the new pressure variable $P = p - \alpha y^2/2$, we finally obtain the system of equations

$$\frac{\partial \mathbf{u}}{\partial t} - \sqrt{\frac{Pr}{Ra}} \Delta \mathbf{u} + \nabla \cdot (\mathbf{u} \otimes \mathbf{u}) + \nabla P = \theta \mathbf{e_2} \tag{20}$$

$$\nabla \cdot \mathbf{u} = 0 \tag{21}$$

$$\frac{\partial \theta}{\partial t} - \frac{1}{\sqrt{Ra\,Pr}} \Delta \theta + \psi_\gamma(x)(\nabla \cdot (\mathbf{u}\theta) + \alpha v) = 0 \tag{22}$$

$$\mathbf{u}(\mathbf{x}, 0) = \mathbf{0}, \quad \theta(\mathbf{x}, 0) = 0 \tag{23}$$

which is supplemented with

$$\mathbf{u}(\mathbf{x}, t) = 0, \quad \mathbf{x} \in \Gamma \tag{24}$$

$$\theta(\mathbf{x}, t) = \frac{1}{2}\left(\tanh\left(\frac{2x+1}{2\zeta}\right) - \tanh\left(\frac{2x-1}{2\zeta}\right) \right), \quad \mathbf{x} \in \Gamma_0 = \{\mathbf{x} \in \Gamma;\ y = 0\} \tag{25}$$

$$\theta(\mathbf{x}, t) = 0, \quad \mathbf{x} \in \Gamma \setminus \Gamma_0 \tag{26}$$

In the following section, the numerical approximation of (20)–(26) is addressed.

4. NUMERICAL APPROXIMATION

The numerical discretization of (20)–(26) is achieved by using a second-order projection scheme in time coupled with a second-order finite volume approximation in space. The unknowns are placed on a staggered mesh as for the classical MAC scheme [16].

4.1. Time discretization

The natural convection problem (20)–(26) is solved in two steps decoupling the computation of the temperature fluctuation and of the velocity–pressure unknowns. A second-order projection scheme [17–19] is first applied to solve the momentum equations (20) and to enforce the incompressibility constraint (21).

Let $\delta t > 0$ stand for the time step and $t^k = k\delta t$ discrete time values. Let us consider that $(\mathbf{u}^j, P^j, \theta^j)$ are known for $j \leqslant k$. The computation of $(\mathbf{u}^{k+1}, P^{k+1})$ consists in:

- Computing a predictor $\widetilde{\mathbf{u}}^{k+1}$ by solving

$$\frac{\widetilde{\mathbf{u}}^{k+1} - \mathbf{u}^k}{\delta t} - \sqrt{\frac{Pr}{Ra}} \Delta\left(\frac{\widetilde{\mathbf{u}}^{k+1} + \mathbf{u}^k}{2}\right) + \nabla P^k$$
$$= \frac{1}{2}(3\theta^k - \theta^{k-1})\mathbf{e}_2 - \frac{3}{2}\nabla\cdot(\mathbf{u}^k \otimes \mathbf{u}^k) + \frac{1}{2}\nabla\cdot(\mathbf{u}^{k-1} \otimes \mathbf{u}^{k-1}) \tag{27}$$

$$\widetilde{\mathbf{u}}^{k+1} = \mathbf{0} \quad \text{on } \Gamma \tag{28}$$

- Projecting to obtain a divergence free velocity $\mathbf{u}^{k+1}$:

$$\frac{\mathbf{u}^{k+1} - \widetilde{\mathbf{u}}^{k+1}}{\delta t} + \frac{1}{2}\nabla(P^{k+1} - P^k) = 0 \tag{29}$$

$$\nabla\cdot\mathbf{u}^{k+1} = 0, \quad \mathbf{u}^{k+1}\cdot\mathbf{n} = 0 \quad \text{on } \Gamma \tag{30}$$

Finally, the temperature variation θ^{k+1} is computed by solving

$$\frac{\theta^{k+1} - \theta^k}{\delta t} - \frac{1}{\sqrt{Ra\,Pr}}\Delta\left(\frac{\theta^{k+1} + \theta^k}{2}\right)$$
$$= -\psi_\gamma(x)\left(\frac{3}{2}(\nabla\cdot(\mathbf{u}^k\theta^k) + \alpha v^k) - \frac{1}{2}(\nabla\cdot(\mathbf{u}^{k-1}\theta^{k-1}) + \alpha v^{k-1})\right) \tag{31}$$

$$\theta^{k+1} = \frac{1}{2}\left(\tanh\left(\frac{2x+1}{2\zeta}\right) - \tanh\left(\frac{2x+1}{2\zeta}\right)\right) \text{ on } \Gamma_0, \quad \theta^{k+1} = 0 \quad \text{on } \Gamma\backslash\Gamma_0 \tag{32}$$

Hence, viscous and diffusion terms are discretized with the Crank–Nicolson scheme, whereas nonlinear convective terms are integrated by the second-order Adams–Bashforth scheme. Scheme (27)–(32) is globally second-order accurate. This semi-implicit/explicit approach is frequently used (see, for instance, [20, 21]) for the time discretization of the Navier–Stokes equations and is well suited especially when time-dependent solutions are computed. As pointed out in [22], second-order projection methods are not appropriate for seeking steady-state solutions with *large*

time steps. Note that due to the explicit treatment of the convective terms, the time step is limited here by a Courant–Friedrichs–Lewy (CFL) condition and is therefore *relatively* small. The approximate stationary solutions obtained by using (27)–(32) may depend on the time step due to the discretization error (see [23]) of the splitting scheme. Therefore, special care is required when the spatial discretization and the stationarity criterion are defined so that these errors become negligible.

Finally, note that the temperature is computed once the projected (divergence-free) velocity is obtained. A different approach is used in [9, 15, 24]: the temperature is first computed; then the velocity field is obtained by using the temperature at the new time level. As we will see in Section 5.1, both time-stepping schemes achieve a second-order accuracy and provide similar results. In addition, in [9, 24], a BDF projection scheme is implemented to discretize the advection–diffusion terms. The BDF scheme may be more efficient for the computation of nonstationary solutions as it provides a more accurate approximation of the pressure. In the case of stationary solutions, which are our main concern in this paper, the more classical approach used here provides satisfactory results.

4.2. Space discretization

4.2.1. Mesh and unknown locations.
Owing to the combined effects of the gravity force and the vertical stratification, flow variables decay rapidly with respect to the vertical elevation. Therefore, the domain Ω is discretized by using a uniform subdivision in the y-direction. A nonuniform grid is required in the x-direction as $L \gg H$. Let N and M denote two integers and let

$$x_i = \frac{L}{2}\varphi(i\ell) \quad \text{for } i = 0, \dots, N, \quad \ell = \frac{L}{N}$$

$$y_j = jh \quad \text{for } j = 0, \dots, M, \quad h = \frac{H}{M}$$

The mesh density function φ is defined by

$$\varphi(x) = \frac{2x - L + \gamma_1 \tanh(\gamma_2 x) - \gamma_1 \tanh(\gamma_2(L-x))}{L + \gamma_1 \tanh(\gamma_2 L)} \tag{33}$$

for $x \in (0, L)$. Note that φ takes its values in $(-1, 1)$. With this distribution of the grid points in the horizontal direction, the steps $\ell_i = x_i - x_{i-1}$ increase within the distance from the center of the heated element. The parameters γ_1 and γ_2 are chosen so that the lengths ℓ_i are of order h in the neighborhood of the heated plate $Q = (-\frac{1}{2}, \frac{1}{2})$.

We introduce points $x_{i+1/2} := (x_i + x_{i+1})/2$ for $i = 0, \dots, N-1$, and $y_{j+1/2} := (y_j + y_{j+1})/2$ for $j = 0, \dots, M-1$. All terms in Equations (27), (29), (30) and (31) are discretized in space by using second-order centered finite volume schemes. The discrete unknowns are given on a staggered grid (see [16]): discrete pressure values are located at the center of mesh cells $K_{i-1/2,j-1/2} = (x_{i-1}, x_i) \times (y_{j-1}, y_j)$, vertical velocity and temperature values are located at the center of mesh cells $K_{i-1/2,j} = (x_{i-1}, x_i) \times (y_{j-1/2}, y_{j+1/2})$, and those of the horizontal velocity are located at the center of mesh cells $K_{i,j-1/2} = (x_{i-1/2}, x_{i+1/2}) \times (y_{j-1}, y_j)$, as it is shown in Figure 3. We define the vector $\mathbf{u}^{k+1} \in \mathbb{R}^{(N-1)M}$ of components u_{ij}^{k+1} and similarly, $\mathbf{v}^{k+1} \in \mathbb{R}^{N(M-1)}$, $\mathbf{P}^{k+1} \in \mathbb{R}^{(N-1)(M-1)}$ and $\boldsymbol{\theta}^{k+1} \in \mathbb{R}^{N(M-1)}$ of components v_{ij}^{k+1}, P_{ij}^{k+1} and θ_{ij}^{k+1}, respectively.
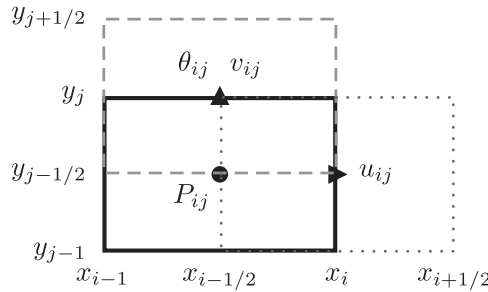
Figure 3. Cells $K_{i-1/2,j-1/2}$ (solid), $K_{i-1/2,j}$ (dashed) and $K_{i,j-1/2}$ (dotted)
and their corresponding discrete values.

In [9], the discrete temperature is located at the pressure nodes $(x_{i-1/2}, y_{j-1/2})$. However, this choice implies interpolations in order to compute the contribution of temperature in the vertical velocity momentum equation and *vice versa*. A more convenient choice for natural convection problems is to place temperature at the same nodes as the vertical velocity.

4.2.2. Discrete systems. The discretization of (27) is achieved by integration of the equation of the horizontal (respectively, vertical) velocity component over the volume cells $K_{i,j-1/2}$ (respectively, $K_{i-1/2,j}$). Gradient and Laplace operators are classically approximated by centered second-order finite volume schemes. Approximation of the nonlinear terms requires second-order interpolations of velocity components at the interfaces; for instance, we use

$$\int_{y_{j-1}}^{y_j} u^2(x_{i-1/2}, y)\,\mathrm{d}y \approx h\left(\frac{u_{ij}^2 + u_{i-1,j}^2}{2}\right)$$

and

$$\int_{x_{i-1/2}}^{x_{i+1/2}} (uv)(x, y_j)\,\mathrm{d}x \approx \left(\frac{u_{ij} + u_{i+1,j}}{2}\right)\frac{(\ell_{i+1} v_{ij} + \ell_i v_{i+1,j})}{(\ell_{i+1} + \ell_i)}$$

Similar interpolation rules are also applied to discretize the equation satisfied by the vertical velocity v. This leads to the system of equations

$$\widetilde{\mathbf{u}}^{k+1} + \frac{\delta t}{2}\sqrt{\frac{Pr}{Ra}}A_1\widetilde{\mathbf{u}}^{k+1} = -\delta t\, G_1\mathbf{P}^k + \mathbf{u}^k - \frac{\delta t}{2}\sqrt{\frac{Pr}{Ra}}A_1\mathbf{u}^k$$
$$-\frac{\delta t}{2}(3N_1(\mathbf{u}^k, \mathbf{v}^k) - N_1(\mathbf{u}^{k-1}, \mathbf{v}^{k-1})) \tag{34}$$

$$\widetilde{\mathbf{v}}^{k+1} + \frac{\delta t}{2}\sqrt{\frac{Pr}{Ra}}A_2\widetilde{\mathbf{v}}^{k+1} = -\delta t\, G_2\mathbf{P}^k + \mathbf{v}^k - \frac{\delta t}{2}\sqrt{\frac{Pr}{Ra}}A_2\mathbf{v}^k$$
$$-\frac{\delta t}{2}(3N_2(\mathbf{u}^k, \mathbf{v}^k) - N_2(\mathbf{u}^{k-1}, \mathbf{v}^{k-1}))$$
$$+\frac{\delta t}{2}(3\boldsymbol{\theta}^k - \boldsymbol{\theta}^{k-1}) \tag{35}$$

where matrices A_i are discrete approximations of the operator $-\Delta$ with appropriate treatment of the boundary conditions for the velocity components, G_i are the ones of the gradient components and N_i are the ones of the nonlinear terms.

With the use of the staggered implementation of the discrete values on the mesh, several possibilities are offered for the treatment of boundary conditions. Concerning the vertical velocity component, we choose to impose the boundary conditions on vertical boundaries at grid points $\{(x_0, y_j), j=1,\ldots,M-1\}$ and $\{(x_N, y_j), j=1,\ldots,M-1\}$. This yields a modified formula for the discretization of $\partial^2 v/\partial x^2$ at the first point away from the vertical boundary, that is

$$\int_{K_{1/2,j}} \frac{\partial^2 v}{\partial x^2}(x,y)\,\mathrm{d}x\,\mathrm{d}y \approx h\left(\frac{v_{3/2,j}-v_{1/2,j}}{x_{3/2}-x_{1/2}} - \frac{v_{1/2,j}-v_{0,j}}{x_{1/2}-x_0}\right)$$

A similar formula applies at the last inner point in the horizontal direction, that is, $x_{N-1/2}$. On horizontal boundaries, boundary conditions for v are imposed at points $\{(x_{i-1/2}, y_0), i=1,\ldots,N\}$ and $\{(x_{i-1/2}, y_M), i=1,\ldots,N\}$. In the vertical direction, the use of second-order centered formula and of uniform mesh points allows us to apply a discrete Fourier transform [25]. We thus obtain a set of independent and symmetric tridiagonal systems that can be efficiently solved with the $\mathrm{LDL}^{\mathrm{T}}$ algorithm.

Boundary conditions for u on the vertical boundaries are also imposed at mesh points, that is, $\{(x_0, y_{j-1/2}), j=1,\ldots,M\}$ and $\{(x_N, y_{j-1/2}), j=1,\ldots,M\}$. However, at the top and bottom horizontal boundaries, values at *ghost points* $y_{-1/2}=-h/2$ and $y_{M+1/2}=H+h/2$ are used to impose boundary conditions with a second-order extrapolation formula: we introduce *ghost* velocity values

$$u_{i,-1}=-u_{i,1} \quad \text{and} \quad u_{i,M+1}=-u_{i,M} \ \text{ for } i=1,\ldots,N$$

The discretization of $\partial^2/\partial y^2$ on the sequence of mesh points $y_{1/2},\ldots,y_{M-1/2}$ with a second-order centered finite volume scheme also yields a discrete operator that can be easily diagonalized by applying a discrete Fourier transform [25].

The discrete version of (29) is obtained similarly

$$\mathbf{u}^{k+1} = \widetilde{\mathbf{u}}^{k+1} - \frac{\delta t}{2}G_1\boldsymbol{\phi}^{k+1}$$

$$\mathbf{v}^{k+1} = \widetilde{\mathbf{v}}^{k+1} - \frac{\delta t}{2}G_2\boldsymbol{\phi}^{k+1}$$

(36)

where $\boldsymbol{\phi}^{k+1}=\mathbf{P}^{k+1}-\mathbf{P}^k$. Note that due to the staggered locations of the unknowns, no boundary conditions for the pressure are required in the correction step (36). Therefore, discrete pressure is defined only at interior points.

The discretization of the incompressibility constraint is achieved by integrating (30) over the pressure cell $K_{i-1/2,j-1/2}$, leading to

$$D_1\mathbf{u}^{k+1} + D_2\mathbf{v}^{k+1} = 0$$

(37)

where D_1 and D_2 are approximations of $\partial/\partial x$ and $\partial/\partial y$. Combining (36) and (37), we deduce the linear system satisfied by $\boldsymbol{\phi}$, namely

$$(D_1G_1+D_2G_2)\boldsymbol{\phi}^{k+1} = -\frac{2}{\delta t}(D_1\widetilde{\mathbf{u}}^{k+1}+D_2\widetilde{\mathbf{v}}^{k+1})$$

(38)

Once (38) is solved, the velocity is updated with (36). The linear system defined by (38) can be solved efficiently by applying the same discrete transform used for the vertical velocity component.

The temperature equation (31) is integrated over the volume cells $K_{i-1/2,j}$, leading to

$$\boldsymbol{\theta}^{k+1} + \frac{\delta t}{2\sqrt{Ra\,Pr}} A_2 \boldsymbol{\theta}^{k+1} = \boldsymbol{\theta}^k - \frac{\delta t}{2\sqrt{Ra\,Pr}} A_2 \boldsymbol{\theta}^k$$

$$- \frac{\delta t}{2} \boldsymbol{\psi}_\gamma (3 N_3(\mathbf{u}^k, \mathbf{v}^k, \boldsymbol{\theta}^k) - N_3(\mathbf{u}^{k-1}, \mathbf{v}^{k-1}, \boldsymbol{\theta}^{k-1}))$$

$$- \frac{\alpha \delta t}{2} \boldsymbol{\psi}_\gamma (3\mathbf{v}^k - \mathbf{v}^{k-1}) \tag{39}$$

where $\boldsymbol{\psi}_\gamma = \{\psi_\gamma^{ij}\} \in \mathbb{R}^{N(M-1)}$, $\psi_\gamma^{ij} = \psi_\gamma(x_{i-1/2})$. Boundary conditions for temperature are treated as for the vertical velocity component.

5. NUMERICAL RESULTS

The main purpose of this paper is to produce reference stationary solutions for heat island flows at Rayleigh numbers $Ra \leqslant 10^5$. In our study the stratification coefficient α is fixed as $\alpha = 1$. Dependency of solutions upon this parameter will be addressed in further studies.

First, the accuracy of our code is evaluated by computing stationary solutions in a square differentially heated cavity. For this test case, benchmark solutions available in [24] are used for comparison. Then, stationary solutions for flows in a heat island are studied. The methodology used to produce accurate results is detailed and solutions are described and analyzed.

5.1. Validation of the code: the square differentially heated cavity test case

In order to assess the validity of our code and to check the accuracy of the numerical scheme (34)–(39) we have performed numerical simulations of stationary solutions to the square differentially heated cavity for values of the Rayleigh number $Ra = 10^6, 10^7$ and 10^8.

Le Quéré [24] produced accurate benchmark solutions for this problem. In [24], Chebyshev polynomials were used for the spatial approximation and an influence matrix technique was applied in order to enforce the divergence-free condition. Note that this problem, described in [21, 24, 26], differs from the heat island problem by the computational domain and the boundary conditions. However, the discrete system (34)–(39), with $\gamma = 0$ and $\alpha = 0$, applies as well to this test case.

Stationary solutions were obtained on uniform grids, in both horizontal and vertical directions, with mesh sizes decreasing from $\frac{1}{32}$ to $\frac{1}{1024}$. The choice of uniform grids is not optimal for this problem as boundary layers develop along the vertical heated walls: a large number of points is thus required in order to obtain accurate results. Such a choice is, however, convenient and allows us to easily check the code accuracy.

The characteristic values suggested by De Vahl Davis and Jones [26] were computed and compared with those of the benchmark solutions [24]. All these values are recovered and a second-order spatial convergence is obtained (see Figure 4).
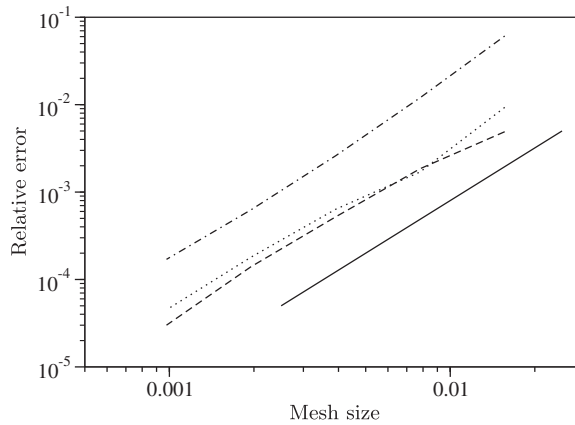
Figure 4. Spatial accuracy for the square differentially heated cavity test case at $Ra = 10^6$. Solid line, slope 2; dashed line, horizontal velocity; dotted line, vertical velocity; dashed-dotted line, Nusselt number.

5.2. Stationary solutions of flows in a heat island

Due to the presence of the vertical stratification, the thermal perturbations are convected in the horizontal direction far from the heated source line. As a consequence, very long domains have to be used in order to produce accurate results. Numerical simulations in small computational domains are contaminated by artificial boundary layers that develop at the outflow boundaries $|x| = L/2$. If the domain length L is not large enough, the temperature cannot smoothly relax toward the vertical stratified profile imposed on the boundaries.

For fixed Rayleigh numbers and mesh sizes, numerical simulations in domains with increasing lengths are performed with the standard heat equation, that is, (31) with $\gamma = 0$. The effects of L and H on the accuracy of the results are investigated. This approach, although time consuming, allows one to produce reference solutions. Numerical simulations with the truncated temperature equation ($\gamma = 1$) are then performed for comparison. This study demonstrates the efficiency of the thermal sponge layers. Finally, stationary solutions at Rayleigh numbers $Ra \leqslant 10^5$ are computed on meshes with a finer resolution. Characteristic values are reported and various profiles are reproduced and analyzed.

The stationary state of the numerical simulations was assumed to be reached when time variations of flow variables are controlled as it follows

$$\max_{n \geqslant 0} \left\{ \frac{|\mathbf{u}^{k+1} - \mathbf{u}^k|_\infty}{\delta t}, \frac{|\mathbf{v}^{k+1} - \mathbf{v}^k|_\infty}{\delta t}, \frac{|\boldsymbol{\theta}^{k+1} - \boldsymbol{\theta}^k|_\infty}{\delta t} \right\} \leqslant \text{Tol}$$

where $\text{Tol} \in (10^{-10}, 10^{-8})$ is a given parameter. When this criterion is satisfied, we have always noted that $|P^{k+1} - P^k|_\infty / \delta t$ is also small. In general, the discrete time variation of the pressure is four orders of magnitude larger than the ones of the velocity components. This criterion not only ensures that the numerical scheme has converged to a discrete *stationary* solution but the numerical solutions were also found to be independent of δt up to the machine accuracy. The time step is chosen so that the numerical stability due to the explicit treatment of the nonlinear terms is ensured: the CFL number is smaller than 0.5.

5.2.1. Numerical simulations in large elongated domains. For fixed vertical resolutions, $h = \frac{1}{16}, \frac{1}{32}$ and $\frac{1}{64}$, and Rayleigh numbers $Ra = 10^3, 10^4$ and 10^5, numerical simulations were performed for increasing values of the height L and length H of the computational domain. The discrete systems (34)–(39) with the parameter γ set to zero was used in order to first test the classical heat equation. The temperature fluctuation θ is the flow variable for which convergence with respect to the domain size is the slowest. Therefore, we choose to use as reference value to compare simulations in different domains the minimum value reached by θ inside the computational domain. Recalling that $\Omega = (-L/2, L/2) \times (0, H)$, we denote

$$\theta_{\min}^{(L,H)} = \min_{(x,y) \in \Omega} \theta(x, y) \tag{40}$$

Note that for stationary solutions, the minimum is reached above the center of the heated element, namely, on the axis $x = 0$ and for $y > 0$. Recalling that the domains are elongated ($L \gg H$) due to the stratified environment, the length L is increased with sufficiently large increments so that significant variations of $\theta_{\min}^{(L,H)}$ are obtained before convergence is reached. We define by

$$\theta_{\mathrm{ref}} = \lim_{(L,H) \to \infty} \theta_{\min}^{(L,H)} \tag{41}$$

In practice, we consider that the above limit is reached when the change in $\theta_{\min}^{(L,H)}$ becomes smaller than $(h^2/10)\theta_{\min}^{(L,H)}$. This convergence criterion is probably too restrictive: even if the numerical spatial accuracy is $O(h^2)$ the constant is often much larger than unity. However, an *a priori* convergence test has to be restrictive in order to ensure accurate results. By performing *a posteriori* comparisons of θ_{ref} for different mesh sizes, we found indeed that the second-order accuracy is recovered. We denote by $(L_{\mathrm{ref}}, H_{\mathrm{ref}})$ the domain sizes found according to the above convergence criterion. Values obtained for the different Rayleigh numbers and mesh sizes are given in Table I. We observe that the domain length L_{ref} is not sensitive to the Rayleigh number, whereas the domain height H_{ref}, for a fixed resolution, decreases when Ra increases. The strength of the stratification grows with the Rayleigh number: the flow is pushed down to the ground.

Table I. Estimate of the size of the computational domain for various mesh sizes h and Rayleigh numbers Ra.

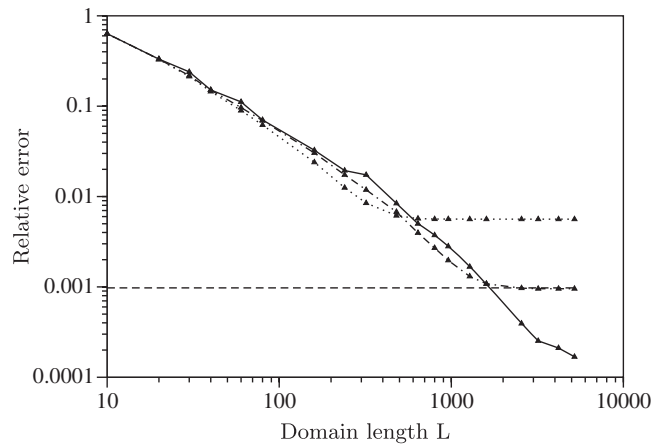| Ra	N_y/H	(L_c, H_c)	$(L_{\mathrm{ref}}, H_{\mathrm{ref}})$
10^3	16	(960, 8)	(3200, 12)
	32	(2560, 10)	(6200, 16)
	64	(5200, 14)	(10 000, 20)
10^4	16	(640, 5)	(3200, 8)
	32	(1920, 6)	(6200, 10)
	64	(4200, 8)	(10 000, 12)
10^5	16	(480, 3)	(3200, 6)
	32	(1280, 4)	(6200, 8)
	64	(3200, 6)	(10 000, 10)

Figure 5. Convergence of $\varepsilon(L, H)$ at $Ra = 10^4$ with respect to the domain length for $H = 4$ (dotted line), $H = 6$ (dotted-dashed line) and $H = 8$ (solid line). The dashed line corresponds to the expected accuracy $h^2 = 1/32^2$.

For (L, H) given, we define a relative error estimate by

$$\varepsilon(L, H) = \frac{|\theta_{\min}^{(L,H)} - \theta_{\mathrm{ref}}|}{|\theta_{\mathrm{ref}}|} \tag{42}$$

For fixed Ra and H, $\varepsilon(L, H)$ is an overall decreasing function. We denote by (L_c, H_c) the minimum domain sizes so that $\varepsilon(L, H)$ becomes smaller than the expected numerical accuracy, namely h^2. Estimates of these minimal values are given in Table I.

Figure 5 represents the convergence history of $\varepsilon(L, H)$ with respect to the domain length L for $H = 4, 6$ and 8. The Rayleigh number is $Ra = 10^4$ and the vertical resolution is $h = \frac{1}{32}$. A rough estimate shows that the convergence rate of the minimum temperature fluctuation toward the reference value θ_{ref} behaves like $L^{-1.2}$. The scheme accuracy is reached for $H = 6$ and L of the order of 2000 (see also Table I). The same behavior with respect to L was found for other vertical resolutions and Rayleigh numbers.

In Figure 6, the convergence history of $\varepsilon(L, H)$ for H fixed to H_c is represented for $Ra = 10^3, 10^4$ and 10^5. The convergence rate of $\varepsilon(L, H)$ is found to be independent of the Rayleigh number: all curves have the same slope in logarithmic scales. In addition, the numerical accuracy $h^2 = 1/32^2$ is reached by $\varepsilon(L, H_c)$ for decreasing values of L when Ra is increased.

For the vertical resolution $h = \frac{1}{64}$, the computation of the reference solution in the domain $\Omega_{\mathrm{ref}} = (0, L_{\mathrm{ref}}) \times (0, H_{\mathrm{ref}})$ with $L_{\mathrm{ref}} = 10\,000$ was achieved with 28\,000 points in the horizontal direction. This guarantees that the mesh satisfies $\ell_i \approx h$ in the neighborhood of the heated element. With the use of the mapping function (33), we have in that case: $\max \ell_i / \min \ell_i = 74$. Therefore, 35.8 (respectively, 17.9) million points were used to compute the reference solution at $Ra = 10^3$ (respectively, 10^5) and 35\,000 (respectively, 200\,000) time iterations were required to reach the stationary solution. This represents 600 (respectively, 1500) monoprocessor computing hours on an IBM Power4 computer.
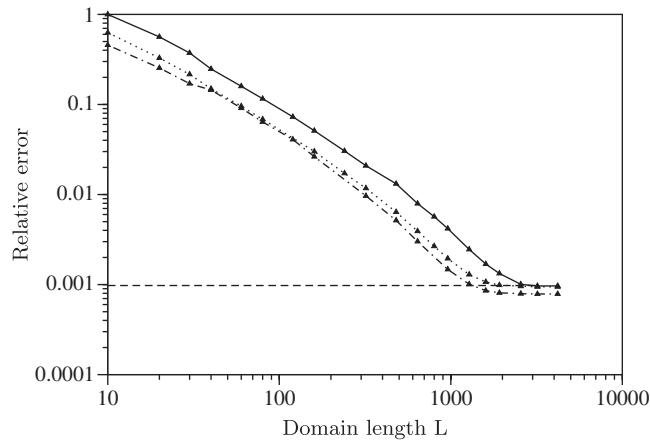
Figure 6. Convergence of $\varepsilon(L, H_c)$ with respect to the domain length for $Ra=10^3$ (solid line), $Ra=10^4$ (dotted line) and $Ra=10^5$ (dashed-dotted line). The dashed line corresponds to the expected accuracy $h^2=1/32^2$.

Owing to this need for a large amount of computational resources, such a study is not feasible on meshes with smaller grid sizes in the vertical direction. By extrapolating the values L_c and H_c found for $h=\frac{1}{16}, \frac{1}{32}$ and $\frac{1}{64}$ (see Table I), we can roughly estimate these minimal values for a finer mesh, namely $h=\frac{1}{128}$. We obtain $(L_c, H_c)=(12\,000, 18)$ at $Ra=10^3$, $(L_c, H_c)=(10\,000, 12)$ at $Ra=10^4$ and $(L_c, H_c)=(8000, 10)$ at $Ra=10^5$. Therefore, a resolution of at least 115 million points would be required in order to compute a reference solution on a grid with a vertical resolution $h=\frac{1}{128}$. As it is shown in the following sections, the use of the truncated heat equation ($\gamma=1$) allows us to significantly relax these constraints on the computational parameters.

5.2.2. Efficiency of the truncated temperature equation. The effect of the filter function (18) is to smoothly damp the convective terms in the heat equation in the vicinity of the domain boundaries $|x|=L/2$. By introducing such thermal sponge layers, we aim at improving the accuracy of the numerical simulations when the computational domains are not long enough to ensure a $O(h^2)$ approximation.

Numerical simulations of stationary solutions at $Ra=10^5$ have been performed with $h=\frac{1}{16}$, $h=\frac{1}{32}$ and $\frac{1}{64}$. The domain height has been fixed at $H=6$. In that case, the errors $\varepsilon(L, 6)$ are dominated by the behavior with respect to L as $H_c=3$ for $h=\frac{1}{16}$, $H_c=4$ for $h=\frac{1}{32}$ and $H_c=6$ for $h=\frac{1}{64}$ (see Table I). The errors $\varepsilon(L, 6)$ produced by the standard and the modified heat equations are used to compare the efficiency of both models. The values $\sigma=0.85$ and $p=8.0$ have been retained for the filter function (18). These parameters were found to be efficient for the numerical simulations of stationary solutions. A parametric study of the truncated temperature equation is beyond the scope of this paper. However, this question is important and will be addressed in future works on this problem.

In Figure 7, the errors $\varepsilon(L, 6)$ obtained for $h=\frac{1}{32}$ with the standard and the truncated heat equations are plotted. The curve corresponding to the truncated heat equation has a very fast decay for small L, namely $L\leqslant 250$. For larger values of L, both curves have similar behaviors.
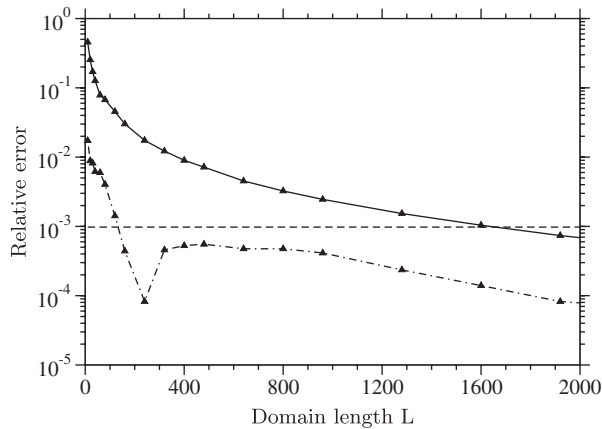
Figure 7. Convergence of $\varepsilon(L, H = 6)$ at $Ra = 10^5$ with respect to the domain length obtained with the standard heat equation (solid line) and the truncated version (dashed-dotted line). The dashed line corresponds to the expected accuracy $h^2 = 1/32^2$.

This indicates that the effects of the nonlinear truncation are stronger on short computational domains. In the region corresponding to $L > 250$, the truncated equation produces errors about 10 times smaller than the standard equation. The error becomes smaller than h^2 for $L \geqslant 160$ when the truncated heat equation is used. With the standard heat equation L has to be larger than 1600 to reach the scheme accuracy (see also Table I).

Recalling that L_c is the minimum domain length necessary to recover the h^2 accuracy, we obtain for L_c the values 40, 160 and 480 with the truncated equation and for the respective resolutions $h = \frac{1}{16}, \frac{1}{32}$ and $\frac{1}{64}$, whereas with the classical heat equation the values 480, 1280 and 3200 are, respectively, found (see Table I).

In addition, by examining the time history of the discrete time variation $|\theta^{n+1} - \theta^n|_\infty / \delta t$, it appears that the convergence to the stationary solution is achieved in less time iterations with the truncated equation than with the classical one. For example, in $\Omega = (-240, 240) \times (0, 4)$ and for $h = \frac{1}{32}$ the stationary solution at $Ra = 10^5$ is reached after 32 000 time iterations with the truncated heat equation, whereas 48 000 time iterations are needed with the classical one (see Figure 8).

Therefore, for a given accuracy, stationary solutions can be computed with the truncated heat equation in significantly smaller computational domains than with the classical temperature equation and in less time iterations. This results in the use of less computational resources. As a consequence, this approach allows us to compute stationary solutions on meshes with a finer vertical resolution.

5.2.3. Accurate stationary solutions. Direct numerical simulations at $Ra = 10^3, 10^4$ and 10^5 and with a vertical resolution $h = \frac{1}{128}$ have been performed with the truncated temperature equation. The computational parameters are listed in Table II. The estimates derived in Section 5.2.1 are used to determine the computational domains. In addition, in agreement with the previous section, domain lengths about 3 times smaller than the estimated values are retained.

In order to characterize the stationary solutions, the maximum values of the velocity components (u, v), the temperature variation θ, the vorticity $\omega = \partial v / \partial x - \partial u / \partial y$ and the streamfunction ψ are
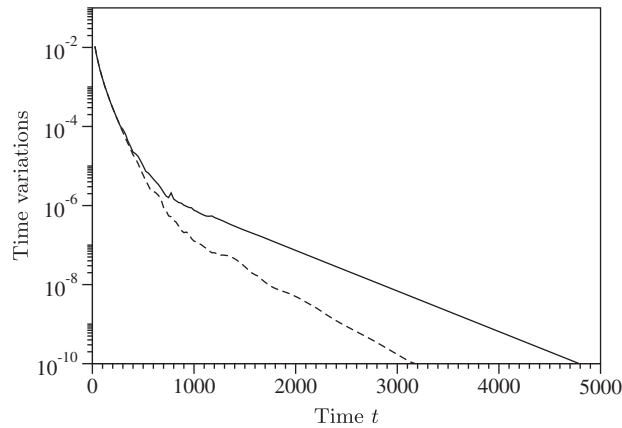
Figure 8. Convergence history of $\max_{i,j} |\theta_{i,j}^{n+1} - \theta_{i,j}^n|/\delta t$ for the standard (solid line) and the truncated (dotted line) heat equations at $Ra = 10^5$. The vertical resolution is $h = \frac{1}{32}$, the time step is $\delta t = 0.1$ and the computational domain is $\Omega = (-240, 240) \times (0, 4)$.

Table II. Computational parameters for numerical simulations on meshes with $h = \frac{1}{128}$.

Ra	10^3	10^4	10^5
(L, H)	$(4400, 18)$	$(3600, 12)$	$(2560, 10)$
(N, M)	$(19\,000, 2304)$	$(16\,500, 1536)$	$(12\,000, 1280)$
δt	0.1	0.05	0.025
T_{stat}	4893	6569	10902

Table III. Characteristic values of the stationary solutions.

| Ra	10^3	10^4	10^5
$\theta_{\min}$	-0.024823	-0.071289	-0.166316
y	1.36191	0.94640	0.84320
$u_{\max}$	0.118887	0.174844	0.179054
(x, y)	$(-0.52314, 0.17705)$	$(-0.36781, 0.13255)$	$(-0.30643, 0.09322)$
$v_{\max}$	0.125594	0.228250	0.322483
y	0.55124	0.44684	0.42552
$v_{\min}$	-0.030470	-0.039291	-0.079265
(x, y)	$(-0.85107, 0.41913)$	$(-0.60361, 0.32122)$	$(-0.39114, 0.64777)$
$\omega_{\max}$	2.06900	3.951325	5.921375
x	0.49642	0.48402	0.47813
$\psi_{\max}$	0.042954	0.048265	0.040272
(x, y)	$(-0.60014, 0.59882)$	$(-0.38883, 0.45575)$	$(-0.25610, 0.45867)$
Nu	0.148605	0.295132	0.643594
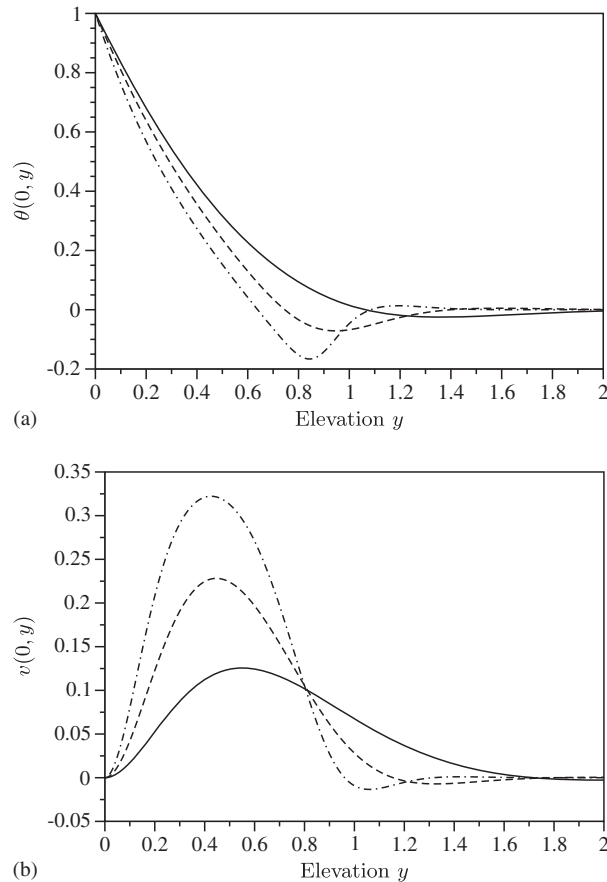
Figure 9. Profiles of the temperature variation θ (a) and of the vertical velocity v (b) at the center of the heated element, i.e. at $x=0$, for $Ra=10^3$ (solid line), $Ra=10^4$ (dashed line) and $Ra=10^5$ (dashed-dotted line). The vertical resolution $h=\frac{1}{128}$ and the truncated heat equation were used.

given in Table III. The locations in the computational domains where these extrema are reached are also collected: when only one of the coordinates is listed, the other one is equal to 0.

Also reported in Table III is the Nusselt number, which is defined by

$$Nu=-\frac{1}{L}\int_{-L/2}^{L/2}\frac{\partial\theta}{\partial y}(x,y=0)\,\mathrm{d}x$$

As expected, this value, which measures the intensity of the heat transfer, increases with the Rayleigh number.

The velocity components and the temperature fluctuation decay rapidly with respect to the elevation y as it is shown in Figures 9 and 11 representing the vertical profiles at the center of the heated element $x=0$. The gravitational force and the vertical stratification limit the vertical propagation of perturbations. In the horizontal direction (see Figure 10(b)), the vertical velocity
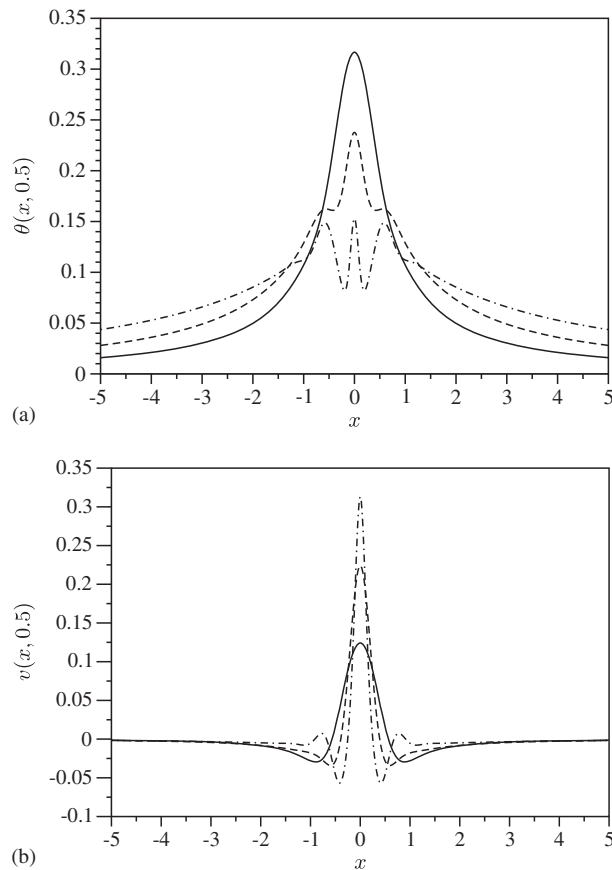
Figure 10. Profiles of the temperature variation θ (a) and of the vertical velocity v (b) at elevation $y = 0.5$, for $Ra = 10^3$ (solid line), $Ra = 10^4$ (dashed line) and $Ra = 10^5$ (dashed-dotted line). The vertical resolution $h = \frac{1}{128}$ and the truncated heat equation were used.

v vanishes rapidly for x outside of the heated region, that is, for $|x| > 0.5$. Therefore, vertical convection is essentially localized above the heated element: this behavior is independent of the Rayleigh number. However, its intensity increases with Ra. Indeed, the maximum value reached by the vertical velocity component increases with Ra (see Figure 10(b) and Table III). The temperature fluctuation and the horizontal velocity have a similar behavior in the horizontal direction for $|x| \geqslant 2$ (see Figures 10(a) and 12): they decay slowly to a small but nonzero value, which grows with Ra. Therefore, the convection outside the heated source line is mainly horizontal. This illustrates the difficulty in approximating such flows in limited computational domains.

The profiles of the temperature fluctuation, plotted in Figures 9(a) and 10(a), show that the ascending propagation of the thermal perturbation is reduced when Ra is increased. Simultaneously, the profile of the velocity components exhibit largest extrema and steepest gradients for $y \leqslant 1$ (see Figures 9(b) and 11). In addition, elevations where the velocity components are maximum decrease for growing Ra (see Table III). Hence, when the Rayleigh number is increased, the flow is pushed
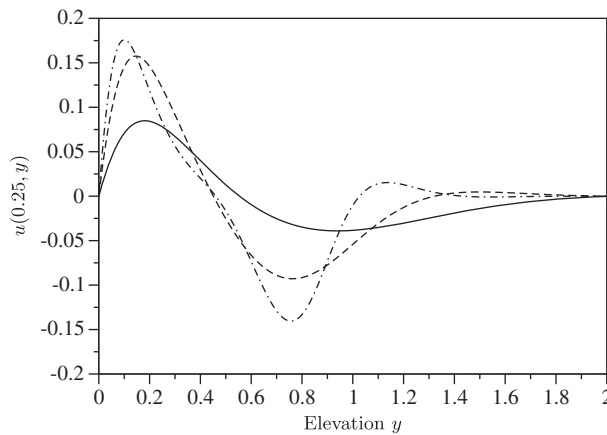
Figure 11. Profile of the horizontal velocity u at $x=0.25$ for $Ra=10^3$ (solid line), $Ra=10^4$ (dotted line) and $Ra=10^5$ (dashed line). The vertical resolution $h=\frac{1}{128}$ and the truncated heat equation were used.
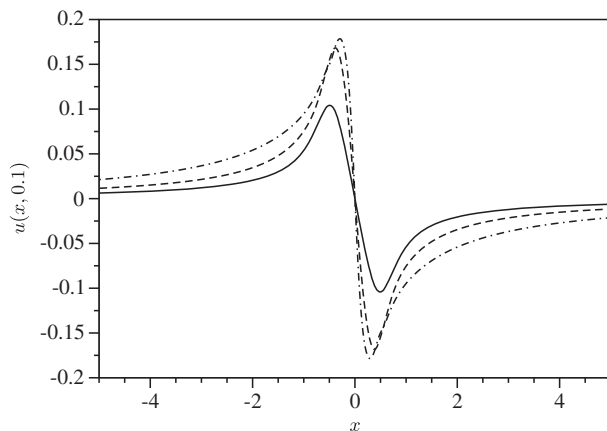

Figure 12. Profile of the horizontal velocity u at elevation $y=0.1$ for $Ra=10^3$ (solid line), $Ra=10^4$ (dotted line) and $Ra=10^5$ (dashed line). The vertical resolution $h=\frac{1}{128}$ and the truncated heat equation were used.

down to the ground. At larger Rayleigh numbers, we expect that the competition between the natural convection, inducing an ascending propagation, and the vertical stratification, limiting this effect, will induce a loss of symmetry of the solutions leading to unsteady flows.

To better illustrate the effect of the vertical stratification, isolines of the temperature fluctuation θ and the vorticity ω are displayed in Figures 13 and 14 in a region surrounding the heat island perturbation, that is, for $|x|\leqslant5$ and $y\leqslant3$. The thermal plume in the form of a mushroom, typical in natural convection problems (see [8], for instance), cannot develop in a stratified medium. Instead, the main thermal structure is centered above the heated plate, symmetric with respect to the axis $x=0$ and very elongated in the horizontal direction. Above, a thermal sink characterized by negative temperature variation θ is observed. The intensity of this structure grows with Ra,
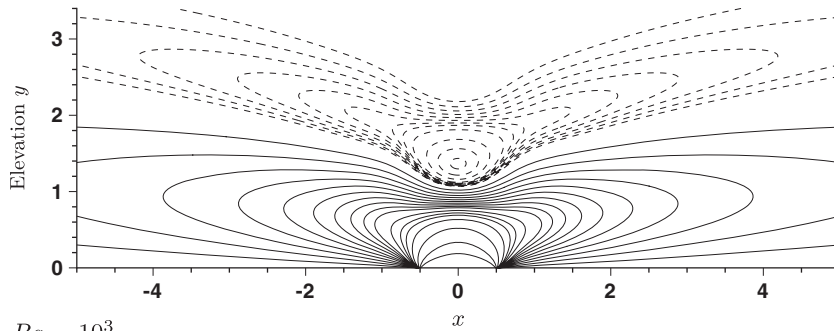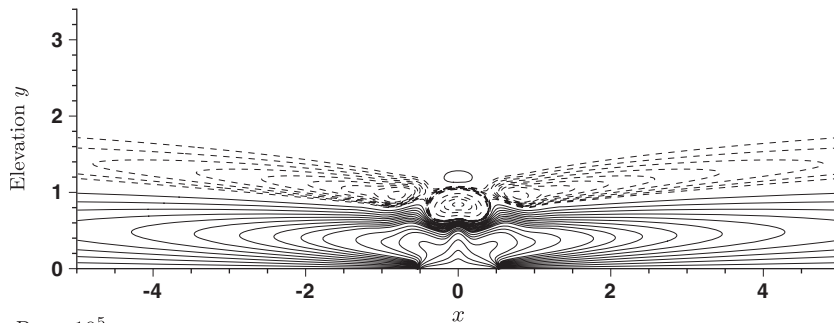
$Ra = 10^3$

Dashed lines: $-0.024, -0.02, -0.015, -0.01, -0.008, -0.007, -0.006, -0.005, -0.004, -0.003, -0.002,$ $-0.001.$
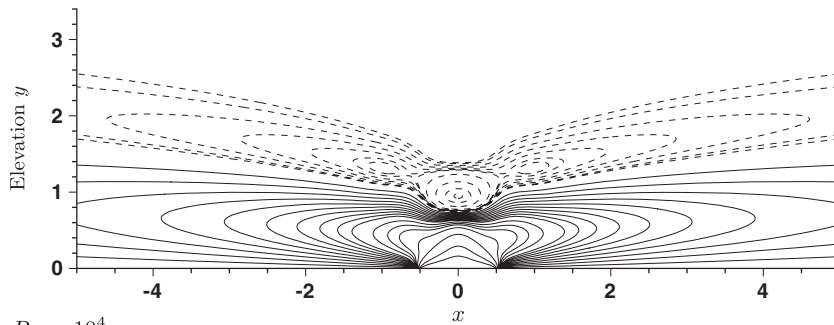
$Ra = 10^4$

Dashed lines: $-0.07, -0.06, -0.04, -0.02, -0.011, -0.01, -0.008, -0.006, -0.004, -0.002, -0.001.$

$Ra = 10^5$

Dashed lines: $-0.16, -0.13, -0.1, -0.06, -0.02, -0.016, -0.014, -0.012, -0.01, -0.008, -0.006, -0.004,$ $-0.002.$

Figure 13. Isolines of the temperature variation for increasing Rayleigh numbers. Solid lines: 0.01, 0.02, 0.03, 0.04, 0.05, 0.06, 0.07, 0.08, 0.09, 0.1, 0.12, 0.14, 0.16, 0.2, 0.3, 0.5, 0.7.

whereas its vertical position decreases. The vorticity structures (see Figure 14) exhibit multi-cell symmetric patterns. They become thinner when Ra increases and are clearly pushed down to the axis $y = 0$.

$Ra = 10^3$

Solid lines: $0.02, 0.03, 0.04, 0.05, 0.06, 0.07, 0.078, 0.1, 0.15, 0.2, 0.3, 0.4, 0.5, 0.6, 1.0$.
Dashed lines are opposite values

$Ra = 10^4$

Solid lines: $0.02, 0.04, 0.06, 0.08, 0.1, 0.15, 0.2, 0.25, 0.3, 0.4, 0.6, 1.0$
Dashed lines are opposite values.

$Ra = 10^5$

Solid lines: $0.01, 0.02, 0.04, 0.06, 0.07, 0.1, 0.15, 0.2, 0.3, 0.4, 0.6, 1, 1.5, 2.0$.
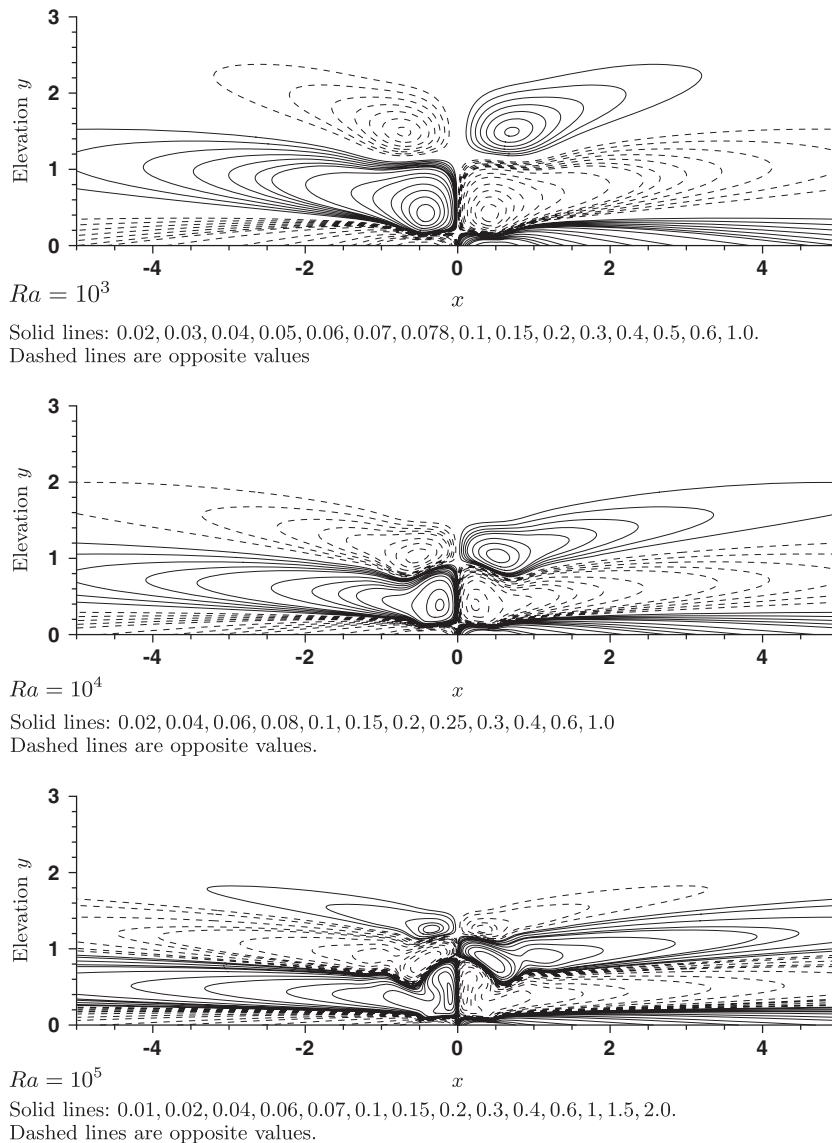Dashed lines are opposite values.

Figure 14. Isolines of the vorticity for increasing Rayleigh numbers.

5.2.4. Computational efficiency. A parallel version of the Fortran 90 code based on implicit communications (OpenMP) was used for the numerical simulations presented in this paper: an efficiency of approximately 6.8 is found on eight processors on a cluster of IBM Power 4 computers. In order to perform the numerical simulations presented in Section 5.2.3, 6000 monoprocessor hours were necessary. The CPU time per iteration and per node used by the code is 2.5×10^{-6} s on IBM Power 4 processors. Concerning the memory, 20 real unknowns (8 bytes) have to be stored for each node of the mesh.

6. CONCLUDING REMARKS AND PERSPECTIVES

In this paper, steady-state solutions of a natural convection problem in an unbounded domain are investigated by direct numerical simulations. For this problem, the flow is thermally stratified in the vertical direction and perturbed by a local heat island located on the ground. Owing to vertical stratification, the flow circulation is dominated by horizontal convection, so that perturbations are propagated in the horizontal direction far from the heated source. Stationary solutions are first investigated by numerical simulations in *very elongated* domains for moderate vertical resolutions, that is, $h = \frac{1}{16}, \frac{1}{32}$ and $\frac{1}{64}$. Repeated computations in increasing domains have been performed: the minimum length and height necessary to ensure a $O(h^2)$ accuracy have been estimated at $Ra = 10^3, 10^4$ and 10^5. This approach, although time and memory consuming, provided reference simulations that have been used to validate and compare results obtained with a truncated heat equation. We have shown that the use of a suitable thermal sponge layer placed at the vertical outflow allows one to noticeably reduce the size of the computational domain. Therefore, numerical simulations on finer grids are made accessible. The stationary solutions at the aforementioned Ra have been computed on grids with vertical resolution $h = \frac{1}{128}$. Characteristic values of these steady states have been provided.

The thermal circulation induced by the heat island consists in symmetric multi-cell pattern centered above the heated element. Flow structures are pushed down to the ground when the Rayleigh number is increased. In addition, their intensity grows with Ra. We therefore may expect that the stability of steady states will be lost at larger Ra leading to nonstationary solutions. The thermal sink found above the heat island should first oscillate with respect to the vertical axis $x = 0$ in a periodic time regime. The numerical study of the development of instabilities and the detection of successive transitions from steady state to turbulent flows is our main motivation. Contributions to this project will be presented in forthcoming papers. Dependency of solutions upon the stratification coefficient is also an open question for this problem. Such a study will be addressed in future works.

REFERENCES

1. Malkus JS, Stern ME. The flow of a stable atmosphere over a heated island, part I. *Journal of Meteorology* 1953; **10**:30–41.
2. Olfe DB, Lee RL. Linearized calculations of urban heat island convection effects. *Journal of Atmospheric Sciences* 1971; **28**:1374–1388.
3. Delage Y, Taylor PA. Numerical studies of heat island circulations. *Boundary-Layer Meteorology* 1970; **1**:201–226.
4. Dubois T, Touzani R. Numerical simulations of thermally stratified flows in an open domain. In *ECCOMAS CFD 2006*, Wesseling P, Onate E, Périaux J (eds). TU Delft: The Netherlands, 2006.
5. Gartling DK. A test problem for outflow boundary conditions—flow over a backward-facing step. *International Journal for Numerical Methods in Fluids* 1990; **11**:953–967.
6. Leone Jr JM. Open boundary condition symposium benchmark solution: stratified flow over a backward-facing step. *International Journal for Numerical Methods in Fluids* 1990; **11**:969–984.

7. Evans G, Poalucci S. The thermoconductive instability of plane Poiseuille flow heated from below: a proposed benchmark solution for open boundary flows. *International Journal for Numerical Methods in Fluids* 1990; **11**:1001–1013.

8. Xin S, Duluc M-C, Lusseyran F, Le Quéré P. Numerical simulations of natural convection around a line-source. *International Journal for Numerical Methods in Fluids* 2004; **14**(7):828–848.

9. Bruneau CH, Saad M. From steady state to chaotic solutions in a differentially heated cavity of aspect ratio 8. *International Journal for Numerical Methods in Fluids* 2002; **40**:1093–1107.

10. Berenger JP. A perfectly matched layer for the absorption of electromagnetic waves. *Journal of Computational Physics* 1994; **114**:185–200.

11. Abarbanel S, Gottlieb D, Hesthaven JS. Non-linear PML equations for time dependent electromagnetics in three dimensions. *Journal of Scientific Computing* 2006; **28**(2–3):125–137.

12. Mahesh K, Lele SK, Moin P. The influence of entropy fluctuations on the interaction of turbulence with a shock wave. *Journal of Fluid Mechanics* 1997; **334**:353–379.

13. Boersma BJ. Numerical simulation of the noise generated by a low Mach number, low Reynolds number jet. *Fluid Dynamics Research* 2004; **35**(6):425–447.

14. Touzani R. Finite element computation of pollutant transport in thermally stratified flows. *Boundary-Layer Meteorology* 1987; **41**:279–285.

15. Xin S, Le Quéré P. An extended Chebyshev pseudo-spectral benchmark for the 8:1 differentially heated cavity. *International Journal for Numerical Methods in Fluids* 2002; **40**:981–998.

16. Harlow FH, Welch JE. Numerical calculation of time-dependent viscous incompressible flow of fluid with free surface. *Physics of Fluids* 1965; **8**(12):2182–2189.

17. Gresho PM. On the theory of semi-implicit projection methods for viscous incompressible flow and its implementation via a finite element method that also introduces a nearly consistent mass matrix. Part 1: theory. *International Journal for Numerical Methods in Fluids* 1990; **11**:587–620.

18. Guermond JL. Some practical implementations of projection methods for Navier–Stokes equations. *Mathematical Modelling and Numerical Analysis* 1996; **30**:637–667.

19. Quarteroni A, Saleri F, Veneziani A. Factorization methods for the numerical approximation of Navier–Stokes equations. *Computer Methods in Applied Mechanics and Engineering* 2000; **188**:505–526.

20. Kim J, Moin P. Application of a fractional-step method to Navier–Stokes equations. *Journal of Computational Physics* 1985; **59**:308–323.

21. Le Quéré P, Alziary De Roquefort T. Computation of natural convection in two-dimensional cavities with Chebyshev polynomials. *Journal of Computational Physics* 1985; **57**:210–228.

22. Gresho PM, Chan ST, Christon MA, Hindmarsh AC. A little more on stabilized Q1Q1 for transient viscous incompressible flow. *International Journal for Numerical Methods in Fluids* 1995; **21**:837–856.

23. Shen J. Hopf bifurcation of the unsteady regularized driven cavity flow. *Journal of Computational Physics* 1991; **95**:228–245.

24. Le Quéré P. Accurate solutions to the square thermally driven cavity at high Rayleigh number. *Computers and Fluids* 1991; **20**(1):29–41.

25. Schumann U, Sweet RA. Fast Fourier transforms for direct solution of Poisson's equation with staggered boundary conditions. *Journal of Computational Physics* 1988; **75**:123–137.

26. De Vahl Davis G, Jones IP. Natural convection in a square cavity: a comparison exercise. *International Journal for Numerical Methods in Fluids* 1983; **3**:227–248.